Effect of Aged Microstructure on the Strength and Work Hardening Behavior of Ti-15V-3Cr-3Sn-3Al Alloy

RAJDEEP SARKAR, A. MUKHOPADHYAY, P. GHOSAL, T.K. NANDY, and K.K. RAY

This investigation is aimed at revealing the deformation behavior of a β-Ti alloy, namely Ti-15V-3Cr-3Sn-3Al, under various aged conditions with an emphasis on correlating the work hardening characteristics of the alloy with its corresponding microstructure. The alloy was cast, forged, hot rolled, solution treated, and aged differently to generate microstructures with varying amounts and morphologies of α- and β-phases. While microstructural characterization was carried out using scanning and transmission electron microscopy (TEM), tensile tests were conducted to study the work hardening behavior of the alloy. One may infer from the results that the strength of the alloy deteriorates, while the elongation to failure improves with an increase in the aging temperature. The strength of the alloy depends strongly on the amount of α- and the inter-α-spacing. The work hardening behavior of the alloy aged at temperatures below 808 K (535 °C) is markedly different than those aged at higher temperatures. This characteristic behavior has been explained using the deformation signatures in the α-phase revealed by TEM examinations. A stress gradient-based model and a dislocation evolution-type model are found to satisfactorily describe the strength and the work hardening behavior of the alloy aged under different conditions.

DOI: 10.1007/s11661-015-2941-1

I. INTRODUCTION

ONE of the commonly used β-Ti alloys, Ti-15V-3Cr-3Sn-3Al (Ti-15-3), has been developed for sheet metal products in various aerospace structural applications, including environmental control system ducts and air-frame brackets.[1,2] The alloy can be heat treated differently to achieve various combinations of strength and fracture toughness for these structural applications. Further, this alloy possesses excellent fabricability and is amenable to the forming of complex parts at room temperature.[2] A considerable amount of work has been done on the microstructural development of the alloy by employing different heat treatments and thermo-mechanical processing to improve its mechanical properties. For example, Ivashin *et al.*[3] have studied the effect of direct aging, cold rolling prior to aging and two–step aging treatment on this alloy and have reported a range of yield strength values from 975 to 1730 MPa. The effect of cold rolling prior to aging[4–6] and the influence of duplex aging on the tensile properties[5,7] of the alloy have also been studied by several other researchers. The effect of varying solutionizing temperatures for this alloy was reported by Okada *et al.*[7] and Fujii and Suzuki;[8] Ma and Wang,[9] and Okada *et al.*[10] have varied the aging temperature, while Kawabe and Munaki[11] have varied the β-grain size, each in order to study the associated effect of that changes in these parameters on the tensile properties. Quiang *et al.*[12] have examined the influence of severely deformed β-grains to nanoscale on the aging behavior and the corresponding tensile properties of the alloy. It can be inferred from the earlier literature that though several attempts have been made in the past to correlate tensile properties with microstructure, there is still considerable lack of information or understanding related to the correlation of the deformation mechanism with the microstructure in this class of alloys. The aim of this report is to examine the inherent operative deformation mechanism from the study of work hardening behavior in relation to the microstructure of an aged β-Ti alloy.

In this investigation, Ti-15-3 alloy is suitably heat treated to understand the effect of aging temperature on the distribution of α and thereby its effect on the mechanical behavior of the alloy. A major emphasis of the work is to gain a better understanding on the mechanism of work hardening behavior of the alloy aged at different temperatures and to correlate these with the corresponding microstructural and sub-structural features.

II. EXPERIMENTAL PROCEDURE

Ti-15V-3Cr-3Al-3Sn alloy was melted using consumable vacuum arc melting. Vanadium was added as a V-Al master alloy, while the other elements were added in pure elemental form. Melting was carried out in a water-cooled

RAJDEEP SARKAR, A. MUKHOPADHYAY, P. GHOSAL, and T.K. NANDY, Scientists, are with the Defence Metallurgical Research Laboratory, Kanchanbagh, Hyderabad 500 058, India. Contact e-mails: rajdeepsarkar@dmrl.drdo.in, rajdeep.sarkar@gmail.com K.K. RAY, Professor, is with the Department of Metallurgical and Materials Engineering, IIT Kharagpur, Kharagpur 721302, India.
Manuscript submitted August 1, 2014.
Article published online May 8, 2015

Table I. Chemical Composition of the Investigated Alloy (in Weight Percent)

Alloy	Al	Cr	Sn	V	C	O	N	H	Ti
Ti-15-3	3.45	3.12	2.84	15.14	0.014	0.12	0.003	0.01	bal.

copper crucible under a vacuum of 10^{-3} mbar. Initially, primary ingots of 10 kg were prepared which were welded and were further re-melted to have a secondary ingot of 20 kg. The skin and the defective portion of the final ingot were discarded. The chemical composition of the alloy is shown in Table I. The ingot was hot forged at 1323 K (1050 °C) followed by hot rolling at 1223 K (950 °C). Specimen blanks from the rolled alloy were solution treated (ST) at 1173 K (900 °C) for 1 hour, followed by water quenching. These specimens were subsequently aged (STA) at 773 K, 808 K, 823 K, and 873 K (500 °C, 535 °C, 550 °C, and 600 °C) for 8 hours, followed by air-cooling. These aged specimens are represented as SA500, SA535, SA550, and SA600 in accordance with their respective aging temperatures. Quantification of aged microstructures was carried out theoretically using Thermo-Calc® software and experimentally by an image processing software, Image tool 3.0. Ultrasonic shear and longitudinal phase velocities were measured in a pulse echo mode using a 200 MHz pulser receiver (Olympus NDT Panametrics PR5900) with 5 and 10 MHz transducers, respectively.

The XRD experiments were carried out using a Philips PW1830 X-ray generator and XRD patterns of the samples were recorded using a step size of 0.015 deg (2θ) and a counting time of 3 s/step. Standard metallographic techniques were used for preparing the samples followed by microstructural characterization using a Quanta 400 (FEI) environmental scanning electron microscope. Orientation image mapping was carried out using a Zeiss SEM (Supra 55) attached with an EBSD detector (Oxford) and the corresponding analysis was performed using '*hkl*' software. Local orientation mapping was carried out using EBSD for sub-grain angles below 5 deg to locate deformed regions in a map. Transmission electron microscopy characterization was carried out using a Tecnai 20T G^2 (FEI) TEM. Foils for TEM investigations were thinned mechanically down to 100 μm followed by electro-polishing. Some parts of the specimens for TEM were also prepared by ion milling.

Tensile properties of the alloy were determined in both the solution-treated as well as in solution-treated plus differently aged conditions. Room temperature tensile tests were performed in a screw driven Instron machine (model: 5500R) at a nominal strain rate of 6.66×10^{-4} s^{-1} using cylindrical specimens of 5-mm gage diameter and 25-mm gage length. In each heat-treated condition, three tensile tests were carried out and the average values of the tensile properties obtained from these tests are reported.

III. RESULTS

A. *Microstructure*

The alloy was solution treated and aged at different temperatures above 773 K (500 °C). The SEM micrographs of the SA500, SA535, SA550, and SA600 specimens are shown in Figure 1. The microstructures in this figure show a two-phase α–β structure in which the α-phase is directly nucleated from the metastable β-phase. The coarsening of the α-precipitates in the microstructures is observed with increase in aging temperatures. It is noted from the SEM images that in addition to change in the size of α, its volume fraction also varies with aging temperature. The volume fraction of α-phase as a function of temperature was theoretically calculated for the temperature range of 473 K to 973 K (200 °C to 700 °C) using Thermo-Calc® software (Figure 2). The results from these calculations reveal that the volume percentage of α increases up to around 623 K (350 °C) and thereafter it decreases with an increase in aging temperature. The volume fraction of the α-phase for the specimens within the investigated aging temperature range, *i.e.,* 773 K to 873 K (500 °C to 600 °C), decreases with aging temperature and the corresponding volume fraction values are summarized in Table II. The observed size of the α-phase is quite fine, but still an attempt was made to measure the volume fraction of this phase from the SEM images using image tool software. The measured percentages of the α-phase are listed in Table II. The results for the volume fraction of the α-phase estimated from quantitative microscopy also depict that it decreases with an increase in aging temperature for the investigated temperature range, similar to the theoretical results obtained by ThermoCalc calculations. A significant difference in the volume fraction values of α-phase is noticed between the theoretical and experimental estimates. This difference can be attributed to two primary reasons: (i) theoretical calculation assumes equilibrium condition for the estimation of the volume fraction of α-phase, which is not true in the experimental case and (ii) the image tool software in experimental estimation could not detect all the α due to its fineness.

X-ray diffraction results for the alloy in the solution-treated and the various solution-treated plus aged conditions are shown in Figure 3. While the solution-treated alloy exhibits only peaks associated with the β-phase, the samples in the aged conditions show peaks of both α-precipitates and β-phase. The ratios between the intensities of (0002) α-peak [$I_{(0002)\alpha}$] and (110) β-peak [$I_{(110)\beta}$] in the X-ray diffraction traces of the differently aged specimens have been determined and are shown in Table II. It is noted that the ratio decreases with an increase in the aging temperature, which is consistent with the reduction in the volume fraction of the α-phase at higher aging temperatures. The width of the α-peaks is also found to decrease with an increase in the aging temperature.

TEM analyses were carried out on samples of all the heat treatment conditions investigated. Bright field

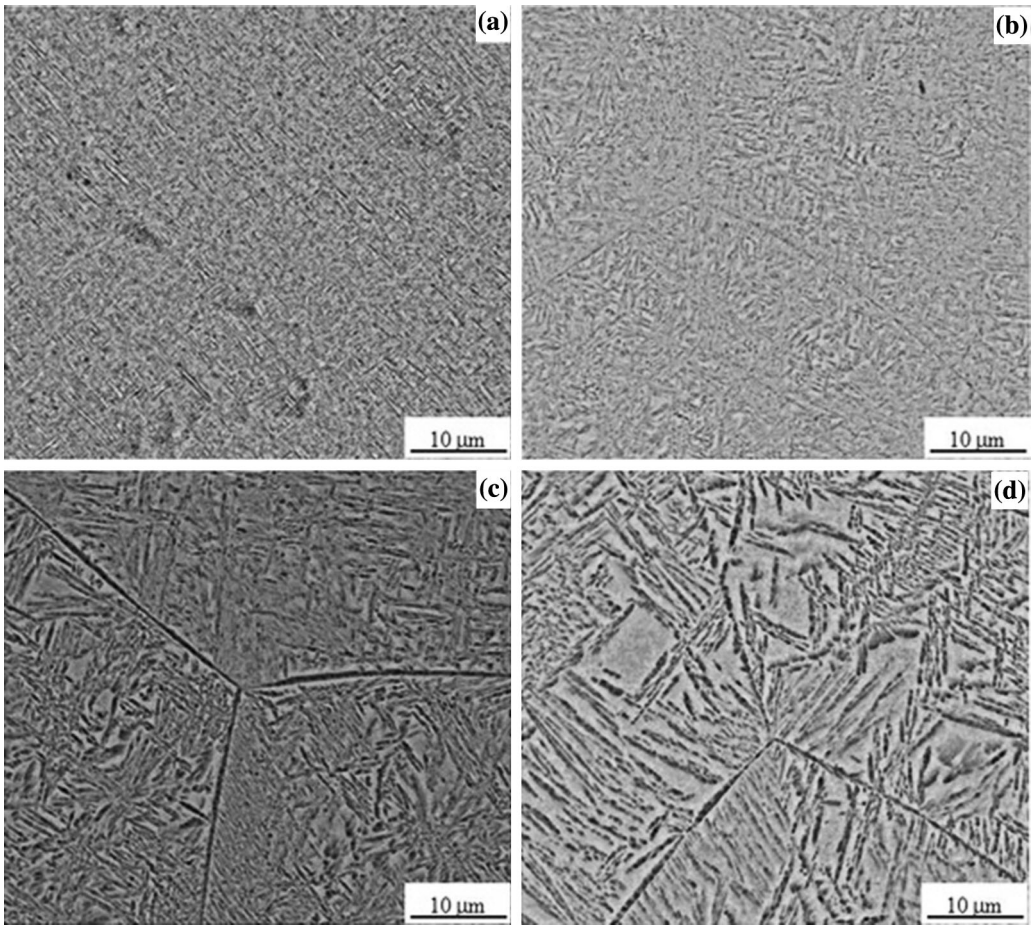

Fig. 1—SEM micrographs of aged specimens (*a*) SA500, (*b*) SA535, (*c*) SA550, and (*d*) SA600 showing the presence of α- (darker contrast) and β-phases (brighter contrast). These exhibit coarsening of α-phase at higher temperature.

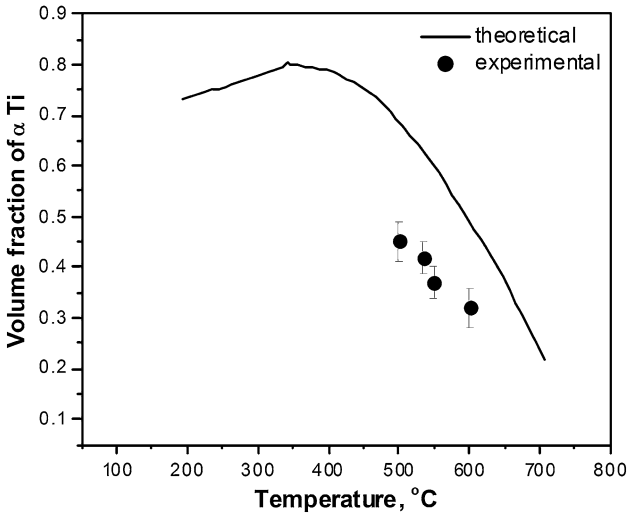

Fig. 2—Variation of volume fraction of α-phase as a function of temperature estimated using Thermo-Calc® software. Experimentally measured values of α-phase from quantitative microscopy are also shown as discrete filled up points.

images after aging at temperatures 773 K and 873 K (500 °C and 600 °C) (Figures 4(a) and (b)), respectively, show that the α-precipitates are coarser at higher aging temperature. The size of these precipitates in the specimens aged between 773 K and 873 K (500 °C and 600 °C), estimated using image tool software from the respective TEM images, are listed in Table II. The average inter-α-spacing in the selected alloys was estimated by considering at least 200 α-laths (aligned as well as randomly oriented) using a number of SEM and TEM BF images and is shown in Table II. The results in Table II show that with a reduction in size and a higher volume fraction of α, the inter-α-spacing decreases for the specimens aged at lower temperatures.

B. *Tensile Properties*

Tensile properties of the alloys in solution-treated and solution-treated plus aged conditions are shown in Figure 5 and in Table III. The elastic modulus value of the solution-treated alloy with a single-phase structure (β) is considerably lower than that of the alloy in the aged conditions. The higher elastic modulus values of the aged specimens are due to the presence of the α-phase; the α-phase possesses higher modulus value than the β-phase.[13] The results in Table III also reveal that the modulus values of the aged specimens decrease with an increase in the aging temperature, as the volume fraction of the α-phase is greater at lower aging

Table II. Volume Fraction, Size, and Inter-Particle Spacing of α-Phase in the Aged Alloys

Sample	$I_{\alpha(0002)}/I_{\beta(110)}$	Volume Fraction of α		Avg. α Size (nm)	Avg. Inter-α-Spacing (nm)
		Image Tool (Percent)	Thermo Calc (Percent)		
SA500	0.24	45 ± 4	68.9	68 ± 20	160 ± 51
SA535	0.23	42 ± 3	62.7	90 ± 30	240 ± 69
SA550	0.22	37 ± 3	59.9	130 ± 60	290 ± 101
SA600	0.14	32 ± 4	49.3	195 ± 55	340 ± 115

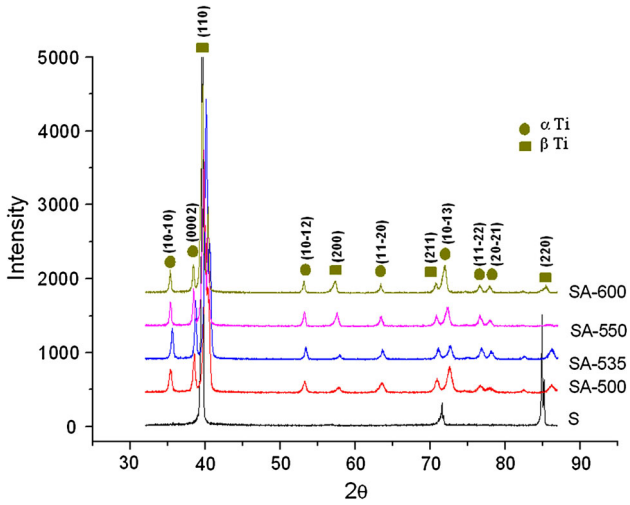

Fig. 3—X-ray diffraction pattern shows peaks of only β-phase in the solution-treated specimen and peaks of both α- and β-phases in the aged specimens.

temperatures (Figure 2). It may be mentioned at this stage that the elastic modulus of the alloy in all the different heat-treated conditions has also been investigated using an ultrasonic method. The elastic modulus values estimated using the stress–strain curves are within 6 pct of their corresponding magnitudes measured by the ultrasonic technique. The yield and tensile strength of the alloy increase after aging as compared to the solution-treated condition; aging beyond 773 K (500 °C) leads to a decrease in strength values. The values of yield strength of the aged alloy have been examined with regard to the inter-α-phase spacing in Figure 6.

The percentage elongation to failure was observed to decrease considerably after aging at 773 K (500 °C) with respect to the solution-treated condition (Figure 5). However, some improvement in elongation is observed for specimens heat treated at higher aging temperatures beyond 773 K (500 °C). Fractographs of the failed tensile specimens aged at 773 K (500 °C) (SA500) and 873 K (600 °C) (SA600) are shown in Figures 7(a) and (b), respectively. While the fractograph of SA500 sample shows fine dimples along with some flat featureless regions or facets, relatively uniform and coarser dimples with higher volume fraction are noticed in the fractograph for the SA600 sample. A longitudinal section of the failed tensile specimen for the alloy aged at 873 K (600 °C) shows the generation of a crack along a grain boundary (Figure 8(a)) and void nucleation at an $\alpha-\beta$ interface (Figure 8(b)). Deformation behavior was also examined using TEM. Dislocation pile up in the β-phase located around the α-phase and deformation of the α-phase in SA500 and SA600 specimens are shown in Figures 9(a) and (b), respectively. Local orientation maps of EBSD images of failed tensile specimens of SA500 and SA600 alloys showing dislocation accumulations around α-phases are revealed in Figures 10((a) and (b)), respectively. The higher density of geometrically necessary dislocations (GNDs) in the SA500 specimen with respect to the SA600 specimen suggests that deformation is confined mostly near the fine α-particles, which are numerous in the SA500 specimen than the SA600 sample.

The calculated true stress values are plotted against the corresponding true plastic strain values in Figure 11 for all the aged conditions. The logarithmic plots of true stress against true plastic strain are shown in Figure 12. These log–log plots (Figure 12) show linear relationships between true stress and true plastic strain values at lower aging temperatures (SA500 and SA535), while a deviation from linearity is seen at higher aging temperatures (SA550 and SA600) suggesting a double-slope behavior. True stress-true plastic strain plots of the aged alloys were examined by fitting to the following expressions[14]:

(i) Hollomon's equation: $\sigma = K\varepsilon^n$
(ii) Double Hollomon-type equation: $\sigma = K_1\varepsilon^{n1} + K_2\varepsilon^{n2}$,
(iii) Ludwingson equation: $\sigma = K_1\varepsilon^{n1} + \exp(K_2 + n_2\varepsilon)$.

The fitting of the expressions to the experimental data has been carried out using the Origin software. The values of n and k obtained from the log–log plots in Figure 12 were used to set the initial values of the parameters in the above expressions for the purpose of fitting. The values of the square of correlation coefficient (r^2 values) for the different types of fitting are shown in Table IV. Plots of work hardening rate ($d\sigma/d\varepsilon_p$) against true stress and true plastic strain are shown in Figures 13(a) and (b), respectively. The results in Figure 13(b) reveal that the initial work hardening rate of the SA500 specimen is higher than that of specimens aged at comparatively higher temperatures. Logarithmic plots of work hardening rate against true stress (Figure 14) are also made using the Crussard–Jaoul (C–J) and modified Crussard–Jaoul (mC–J) analysis[15,16] to study the different

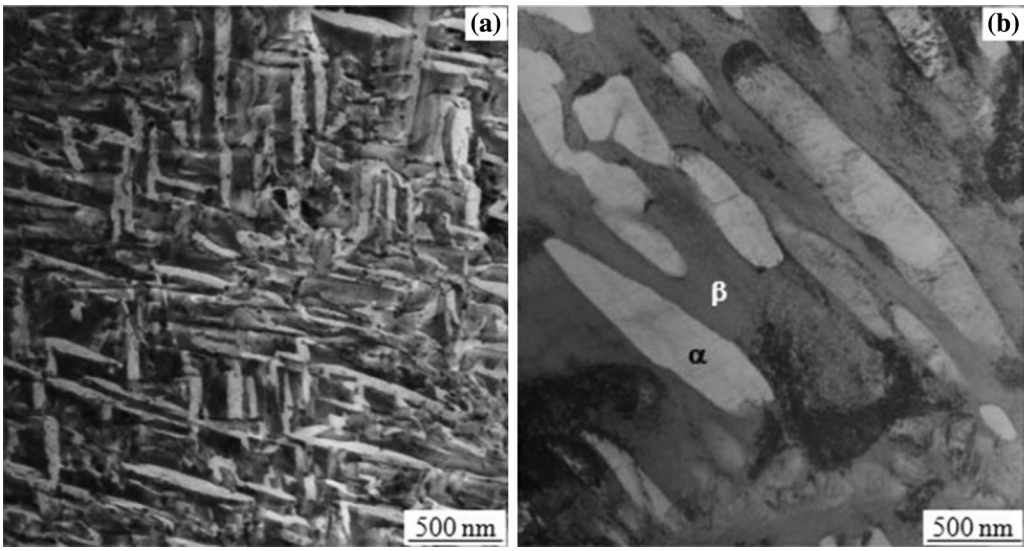

Fig. 4—Typical bright field images of (*a*) SA500 and (*b*) SA600 specimens showing α-laths (bright contrast) in β-matrix (darker contrast). The α-precipitates are coarser at higher aging temperature.

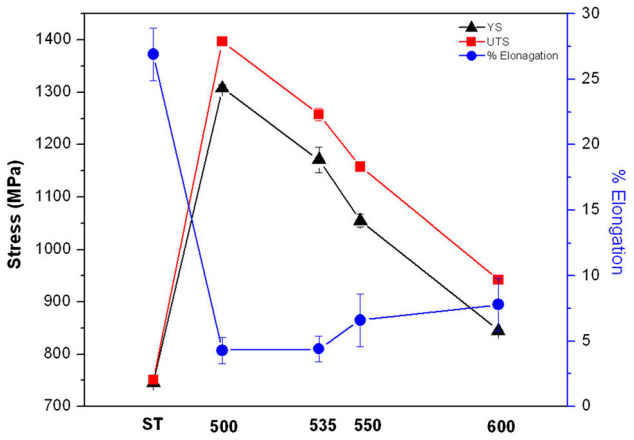

Fig. 5—Variation of yield strength (YS), ultimate tensile strength (UTS), and percentage elongation (pct Elong) with aging temperature. The tensile properties of the solution-treated specimen are also shown.

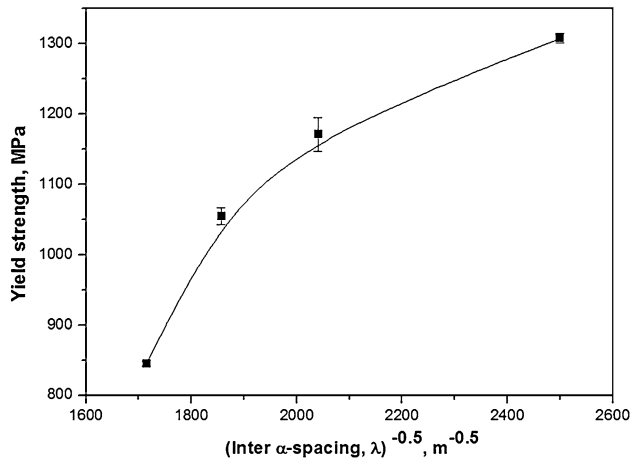

Fig. 6—Plot of yield strength of the aged specimens against inverse square root of inter-α-spacing showing deviation from linearity at smaller inter-α-spacing.

Table III. Tensile Properties of the Solution Treated and Aged Alloy

Sample	YS (MPa)	UTS (MPa)	(Perncet) Strain	Elastic Modulus (GPa)
ST	746 ± 8	751 ± 8	26.9 ± 2	84 ± 1
SA500	1308 ± 7	1397 ± 1	4.1 ± 1	115 ± 2
SA535	1171 ± 24	1258 ± 12	4.4 ± 1	112 ± 3
SA550	1055 ± 12	1158 ± 5	6.6 ± 2	112 ± 0
SA600	845 ± 4	942 ± 7	7.8 ± 2	103 ± 6

stages of work hardening. The work hardening mechanisms in differently heat-treated alloys are discussed by correlating these with the corresponding microstructures.

IV. DISCUSSION

A. *Tensile Properties*

An increase in both yield and tensile strength is observed in the solution-treated alloys aged at 773 K (500 °C) or above. This is due to the presence of fine α in β-matrix resulting in a large number of α–β interfaces that act as obstacles to dislocation motion.[17] With increase in aging temperature from 773 K to 873 K (500 °C to 600 °C), decrease in volume fraction of the α–β interfaces due to coarsening of α (Figures 1 and 4) and reduction in volume fraction of α-phase (Figure 2; Table II) results in decrease in strength. This is well supported by the fact that the plot of yield strength against inverse square root of inter-α-spacing (Figure 6) shows increase in strength with decrease in inter-

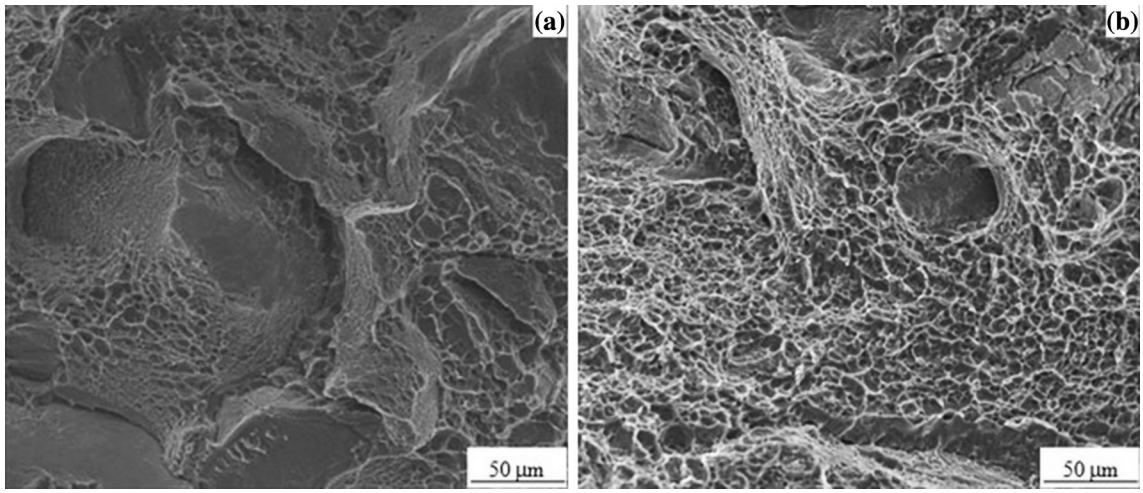

Fig. 7—Fractographs showing (*a*) fine dimples along with some flat featureless regions in SA500 specimen and (*b*) relatively uniform and coarser dimples with lesser extent of flat regions in SA600 specimen.

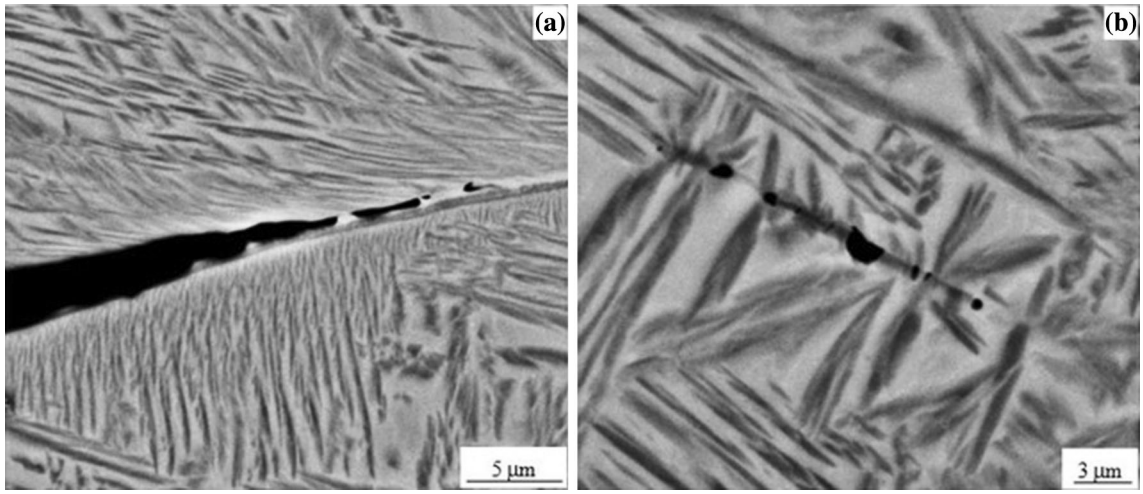

Fig. 8—Typical SEM images of longitudinal section of a failed tensile specimen depicting (*a*) crack along grain boundary and (*b*) void nucleation at the α–β interfaces.

α-spacing. This result shows that inter-particle (in this case fine α) spacing plays significant role in strengthening of these aged alloys.

The relationship between yield strength and inverse square root of inter-α-spacing (Figure 6) is not perfectly linear; it deviates from linearity at smaller inter-α-spacing. Therefore, the dependence of yield strength on inter-α-spacing could not be expressed by a Hall–Petch relationship:

$$\sigma = \sigma_o + k\lambda^{-1/2}, \qquad [1]$$

where σ is yield stress, σ_o is lattice resistance of the matrix, λ is inter-α-spacing, and k is interface strengthening parameter. Further, even if a straight line is drawn forcibly through the experimental points, this relationship results in a negative value of σ_o which does not have any physical significance and obviously indicates the inapplicability of Hall–Petch relationship between σ and λ.

Deviation of the relationship between yield strength and inverse square root of inter-α-spacing (Figure 6) from linearity has invoked us to examine the present result with an alternative model, proposed by Meyers–Ashworth (MA)[18] illustrating the relationship between yield strength and grain size (d). This model, which spans over a large range of grain size, shows $d^{-1/2}$ dependence in relatively coarse grains and d^{-1} dependence in the fine grain range. The increase in yield stress with decreasing grain size is attributed to the formation of work-hardened layers around grain boundary (micro-yielding) due to incompatibility stresses arising from elastic modulus anisotropy. In the present study, the microstructure comprises of α-and β-phases having different elastic moduli. Therefore, the presence of incompatibility stress at the α–β interfaces due to an elastic modulus mismatch cannot be ignored. Finer α-platelets and finer inter-α-spacing in the alloy aged at 773 K (500 °C) as compared to those aged at higher

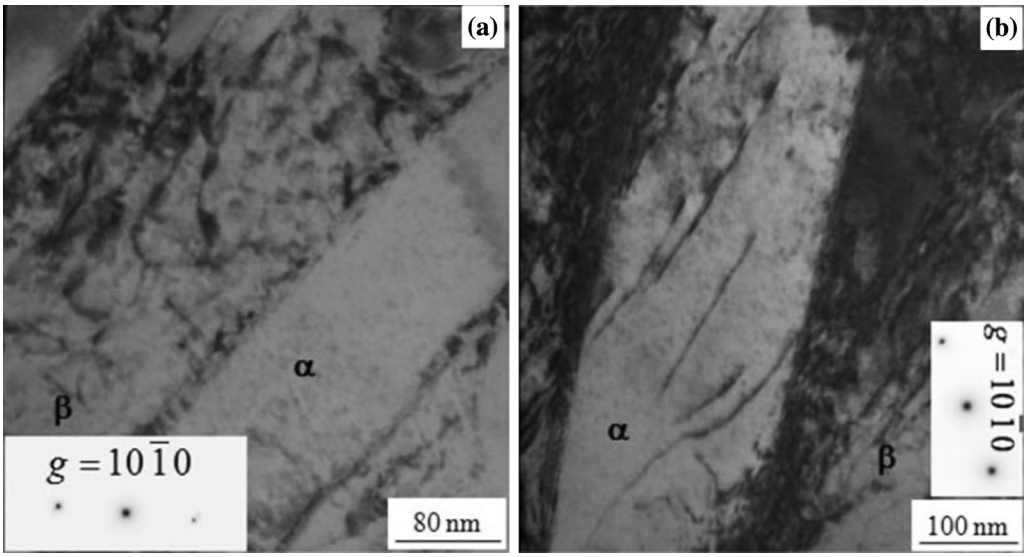

Fig. 9—Typical TEM BF images showing dislocation pile up around α-phase in (*a*) SA500 and (*b*) SA600 specimens. The latter specimen also exhibit signature of deformation in α-phase.

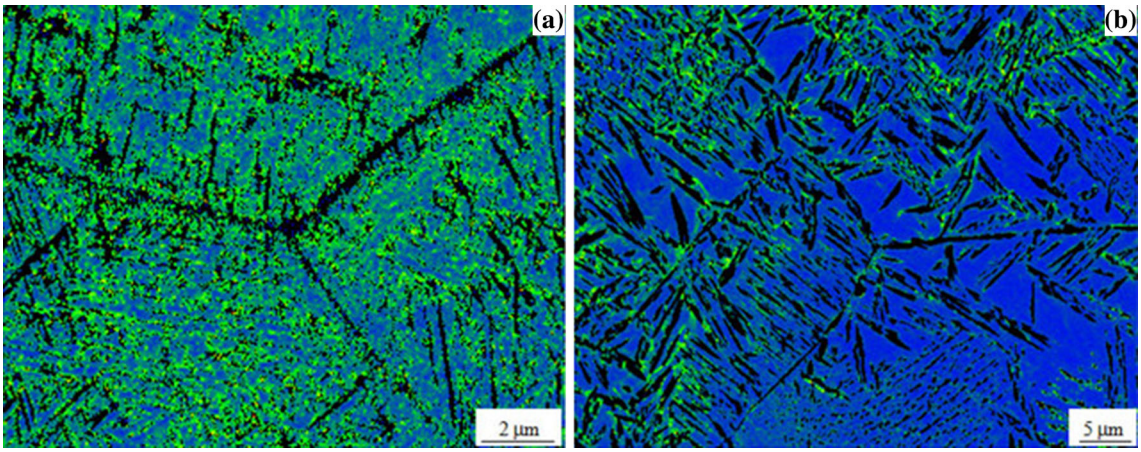

Fig. 10—Local orientation maps of EBSD images of failed tensile specimens of (*a*) SA500 and (*b*) SA600 alloy showing strain or dislocation accumulations (green color) in β-phase (blue color) located primarily around α-phase laths (black color).

temperatures would thus result in a higher contribution from the work-hardened layer, which is considered to explain the higher yield strength observed in the SA500 condition. Therefore, the yield strength dependence on microstructure in the aged conditions can be described by this model. The relationship between yield strength and inverse square root of inter-α-spacing moves toward steady state at finer inter-α-spacing following MA model. Further, the presence of dislocations in the vicinity of α–β interfaces (Figures 9 and 10) points toward the strong possibility that Meyers–Ashworth relationship describes the tensile behavior of the aged β-alloy.

B. *Work Hardening*

True stress-true plastic strain plots of the aged alloys do not follow Hollomon's equation, especially at higher aging temperatures (Table IV). But, when these are plotted following the double Hollomon-type equation or the Ludwingson equation, the fit appears to be better, as indicated by improved r^2 values listed in Table IV. Although these equations result in better curve fitting, the fitting parameters lack any physical significance. Additionally, these cannot be correlated with the microstructure.[19]

The inappropriateness of describing the work hardening behavior by Hollomon or Ludwingson equations leads us to examine the investigated results using C–J and mC–J propositions. The motivation for this analysis originates from the results given in Figure 13(a), where multiple deformation stages are indicated. The C–J analysis and mC–J involve by the logarithmic plots of work hardening rates against true plastic strain and true stress values, respectively, and these are usually considered to reveal the different stages of deformation. The results obtained by C–J and mC–J analysis are illustrated in Figures 14(a) and (b), respectively. A change in

slope in these plots (Figure 14) indicates a change in deformation behavior. The linear regions in the logarithmic plots (Figure 14(b)) revealing different stages of deformation have been marked in relation to the plots of work hardening rates against true stress in Figure 13(a). It must be stated a priori here that the conventional stage-I or II hardening, which are typically observed in single crystals, are not seen here.[20] Results in Figure 14 show regimes of transition from stage II to III and stage-III behavior. A distinct change in the slope (marked as IIIa and IIIb) during stage-III indicates a change in deformation behavior for samples aged at higher temperatures, while those aged at lower temperatures do not show such a change.

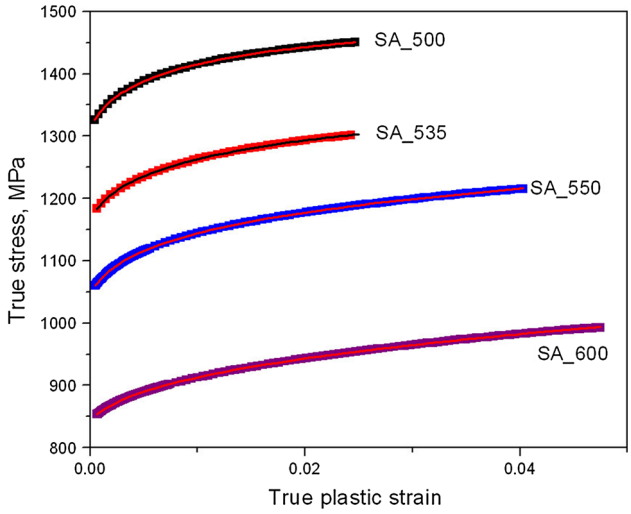

Fig. 11—True stress *vs* true plastic strain plots for the investigated aged specimens. The fitting of these curves by Ludwingson expression is also shown.

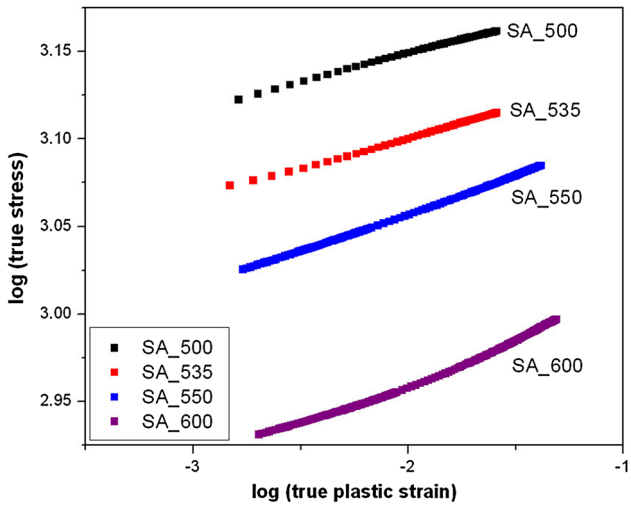

Fig. 12—Logarithmic plots of true stress against true plastic strain for the aged specimens showing nearly linear variation at lower aging temperatures (SA500 and SA535) and double-slope behavior at higher aging temperatures (SA550 and SA600).

The volume fraction of α is considerably high, almost comparable to that of the β-phase, in the alloy aged at lower temperatures. Additionally, α-particles are considerably finer at lower aging temperatures. In the frame work of Meyer–Ashworth model (Section IV–A) and due to assumption of equi-stress conditions, the applied stress initially creates a work-hardened layer in the β-matrix in the immediate vicinity of α–β interface. With increasing stress, the β-phase starts deforming and the presence of this work-hardened layer prevents any slip transfer from β to α. Deformation in the β-phase in the narrow regions between the fine α-particles and almost no deformation in the α-phase result in further strain incompatibility at the α–β interface; this is well corroborated by the EBSD strain maps (Figures 10(a) and (b)). Therefore, the assumption of the equi-stress condition is well supported by the presence of strain gradient at the α–β interface (Figure 10) and insignificant deformation of the α-phase (Figure 9(a)) in SA500 specimens. With continued plastic deformation and a severe strain gradient across α–β interface, void nucleation is expected to occur at α–β interface that subsequently leads to failure by a void coalescence mechanism. Thus, continued deformation in the β-matrix results in the single-slope deformation behavior of low-temperature aged specimens (Figure 14(b)).

On the other hand, at higher aging temperatures, the size of the α-precipitates is coarser and the inter-α-spacing is larger because of the decreasing volume fraction of α. Therefore, in this case, the initial deformation of the alloy is similar to that of the single-phase β that deforms by slip bands and cell formation. Because of the larger slip length (increase in α-spacing), high stress concentration at the tip of pile up leads to slip transfer across the α–β interface at higher strain. Thus, α-phase deformation plays a role in the latter stage of deformation, which possibly results in the observed change of the slope in work hardening plot (stage-IIIb in Figure 14(b)). This is further confirmed by the presence of dislocations in the α-phase (Figure 9). The transition or change over in the slope occurs at around 1.4 pct true

Table IV. Values of Square of Correlation Coefficient (r^2 Values) for Different Types of Fitting

	r^2 Value Associated with Fitting of Different Expressions		
Sample	Hollomon	Ludwigson	Double Hollomon Type
SA500	0.9988	0.99998	0.99999
SA535	0.99867	0.99989	0.99966
SA550	0.99902	0.99999	0.99999
SA600	0.99066	0.99997	0.99998

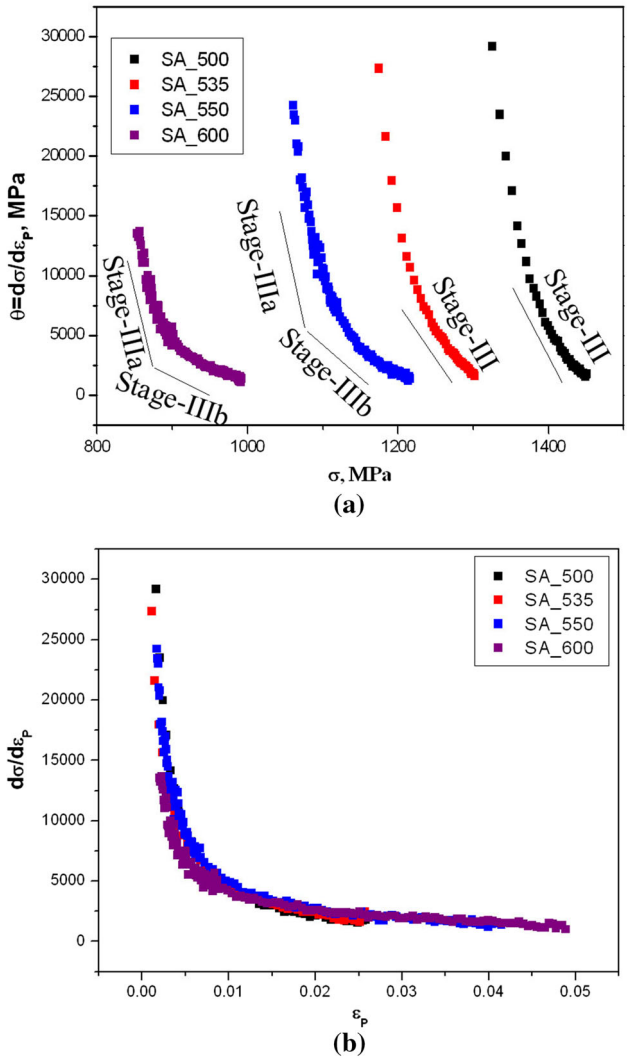

Fig. 13—Plots of work hardening rate (θ) against (*a*) true stress (σ) and (*b*) true plastic strain (ε_p) for all the aged specimens. Regions of stage-III deformation are marked in (a).

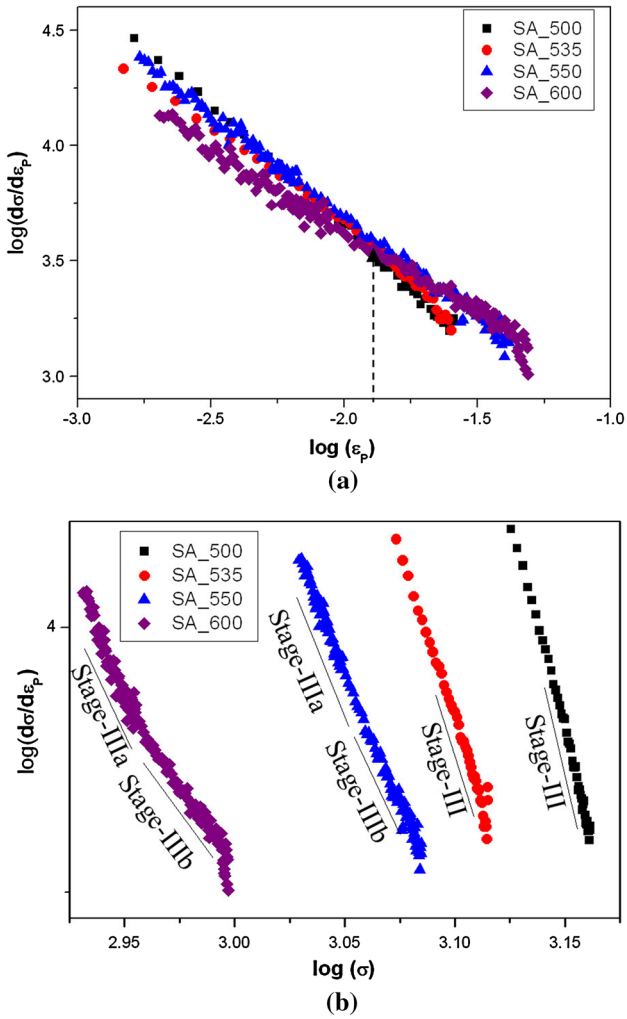

Fig. 14—Logarithmic plots of work hardening rate (θ) against (*a*) true plastic strain (ε_p) and (*b*) true stress (σ) for the aged specimens. The arrow in (a) indicates the strain beyond which SA550 and SA600 specimens show higher work hardening rate than SA500 and SA535 specimens.

plastic strain (Figure 14(a)) and after this transition the deformed α-phase particles result in increased work hardening which is clearly seen in the specimens aged at higher temperature. Finally, at higher strain just before necking the work hardening rate starts to drop rapidly, which is clearly seen for SA600 specimen in Figures 14((a) and (b)). This is attributed to void nucleation and subsequent cracking at prior β-boundaries, which leads to a rapid rate of dislocation annihilation.

The presence of a continuous layer of α at prior β-boundaries (Figure 8(b)) leads to a deterioration in the elongation to failure value of the aged samples. Maximum elongation of about 8 pct is observed in the alloy aged at 873 K (600 °C) as opposed to 27 pct in the single-phase solution-treated alloy. The deterioration in the mechanical properties of a β-Ti alloy because of the presence of continuous α is very well known[21] and the intergranular failure in the fractograph (Figure 7) is consistent with this hypothesis.

The initial work hardening of the specimens aged at lower temperatures (SA500 and SA535) is higher than those aged at higher temperatures, SA550 and SA600, (Figures 11 and 13(b)). The local orientation maps in Figures 10((a) and (b)) show more geometrically necessary dislocations (GNDs) in the SA500 sample after failure and it is considered that these GNDs are also present in higher number in SA500 sample during early stage of plastic flow. These GNDs act as dislocation sources and result in increased number of dislocation interactions causing considerable initial work hardening in this alloy. Considering plate-shaped α-phase, Ashby's[22] equation for plate-like particles is used for the estimation of flow stress of the polycrystalline aged alloys:

$$\sigma = \sigma_o + kM^{3/2}G(b\varepsilon/\lambda)^{1/2}. \quad [2]$$

In the above equation, σ_o is the frictional stress which is considered as the yield strength of the solution-treated alloy, k is a dimensionless constant, M is the average Taylor's factor, G is the shear modulus of the alloy, b is

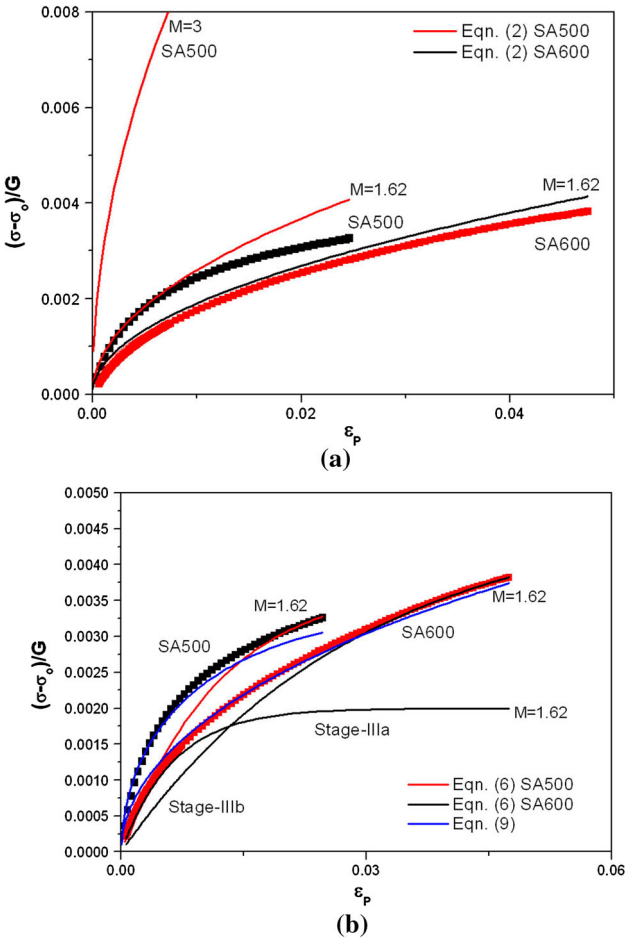

Fig. 15—(*a*) Plots of $(\sigma - \sigma_o)/G$ against strain (ε_p) for SA500 and SA600 specimens together with their predicted values by Ashby's model. (*b*) Variation of $(\sigma - \sigma_o)/G$ against strain (ε_p) for SA500 and SA600 specimens together with their predicted values by Kocks–Mecking and Estrin–Mecking models. The influence of the magnitude of the Taylor's factor (M) is also illustrated in (a).

the Burgers vector of the operating dislocations in the β-matrix phase, λ is the average spacing between two α-laths. The flow stress values of the aged alloys are estimated using Eq. [2] by considering $k = 0.3$, $M = 3$,[23] $b = 0.28$ nm, and the values of λ are taken from Table II; value of the Burgers vector of dislocation, $a/2\langle 1\bar{1}1 \rangle$ is estimated from TEM results. These estimated flow stress values for the SA500 and SA600 samples are examined against strain along with the experimental values in a plot of normalized effective stress, $(\sigma - \sigma_o)/G$, against strain (ε) as shown in Figure 15(a). It can be seen that the theoretical estimates are higher than the experimental values, in which σ_o is considered as the yield stress of the materials. This discrepancy can be attributed to the assumed values of k and M and with the error associated with the estimated value of λ used in the Eq. [2]. Initially, the value of M was varied for better fitting between the estimated and the experiential values. It was observed that the initial parts of the estimated (obtained from Eq. [2]) $(\sigma - \sigma_o)/G$ *vs* strain (ε) curves fitted well with the experimental results for $M = 1.62$, as shown in Figure 15(a). This value of M appears to be significantly lower than that commonly considered for BCC materials. Manipulation of the estimated plots can also be done with variation in the value of k or combined variations of both M and k. But for the convenience of discussion in a simplified manner, the current analysis is limited to only the variation of M. As Eq. [2] considers only the work hardening component (not recovery), the estimated curve for SA500 condition (with $M = 1.62$) starts deviating from the experimental curve (Figure 15(a)) at higher strain. But, this deviation is less for the SA600 condition, as compared to that in the SA500 condition, which implies that moderate hardening may still exist in the later stages in the sample aged at 873 K (600 °C). This hardening stage, marked as Stage-IIIb, can be observed for SA550 and SA600 specimens (Figure 14a) as discussed earlier.

The work hardening due to interaction of dislocations and increase in dislocation density is balanced by dynamic recovery or annihilation of dislocations, which is discussed here in terms of the Kocks–Mecking (KM) model.[20] The KM model interprets the net evolution of dislocation density (ρ) with true plastic strain (ε_p) for polycrystalline material as

$$\frac{d\rho}{d\varepsilon_P} = M(k_1\rho^{1/2} - k_2\rho), \qquad [3]$$

where the first term inside the parenthesis is associated with dislocation storage, which is linked with mean free path or spacing of dislocations, and the latter term is correlated with dynamic recovery, while k_1 and k_2 are corresponding constants. Integration of the Eq. [3][23] represents the dislocation density as

$$\rho^{1/2} = \frac{k_1}{k_2}\left[1 - \left(1 - \frac{k_2}{k_1}\rho_o^{1/2}\right)\exp(-k_2 M\varepsilon/2)\right], \qquad [4]$$

where ρ_o is the initial dislocation density in the undeformed material. Substitution of Eq. [4] in the Taylor's equation[23] relating macroscopic flow stress with dislocation density:

$$\sigma - \sigma_o = kMGb\rho^{1/2} \qquad [5]$$

results in

$$(\sigma - \sigma_o) = kMGb\frac{k_1}{k_2}\left[1 - \left(1 - \frac{k_2}{k_1}\rho_o^{1/2}\right)\exp(-k_2 M\varepsilon/2)\right]. \qquad [6]$$

Differentiation of Eq. [5] with Eq. [3] yields

$$\frac{d\sigma}{d\varepsilon_P} = \theta_o - \beta(\sigma - \sigma_o), \qquad [7]$$

where $\theta_o = (kM^2Gbk_1)/2$ and $\beta = (Mk_2)/2$. Equation [7] represents Stage-III[24] behavior of work hardening phenomenon in polycrystalline materials and indicates linear decrease of work hardening rate with flow stress. The parameter θ_o is considered as an

Table V. Values of the Parameters θ_o and β for all the Aged Specimens

Sample	θ_o (MPa)		β	
	Stage-IIIa	Stage-IIIb	Stage-IIIa	Stage-IIIb
SA500	12,981		84.1	
SA535	11,816		76.6	
SA550	21,284	9942	209	56.1
SA600	12,687	6029	156.6	34.4

θ_o, Athermal hardening coefficient and β, dynamic recovery term in Kocks–Mecking expression.

athermal hardening term and β is related to dynamic recovery. The intercept of the linear Stage-III region with the ordinate axis in $\theta(= d\sigma/d\varepsilon_p)$ *vs* $(\sigma - \sigma_o)$ plot gives θ_o, the initial work hardening rate and the slope of the linear portion corresponds to the value of β. The values of θ_o and β were evaluated from the plots of $\theta(= d\sigma/d\varepsilon_p)$ *vs* $(\sigma - \sigma_o)$ for all the specimens in the differently aged conditions and these are listed in Table V. The results in Table V indicate that for the same stage, *i.e.*, Stage-IIIa for the SA500 and SA535 specimens and Stage-IIIb for SA550 and SA600 samples, values of both θ_o and β decrease with an increase in aging temperature. With these values of θ_o and β, values of k_1 and k_2 were calculated using Eq. [7] for all the aged conditions. With these values of k_1 and k_2, the magnitude of the term $(1 - k_2\rho_o^{1/2}/k_1)$ in Eq. [6] has been considered as unity, as for $\rho_o \sim 10^7$ cm^{-2} $k_2\rho_o^{1/2}/k_1$ tends toward zero. The theoretical values of $(\sigma - \sigma_o)/G$ (estimated using Eq. [6]) considering $k = 0.3$ and $b = 0.28$ nm are plotted against strain together with the experimental results for the alloy aged at 773 K and 873 K (500 °C and 600 °C) (Figure 15(b)).

The predicated values of $(\sigma - \sigma_o)/G$ estimated using Eq. [6] are in good agreement with the experimental ones at higher strain for Stage-III for the SA500 specimen and for the Stage-IIIb for SA600 sample when M is considered as 1.62. This observation together with the earlier one, in which $M = 1.62$, satisfactorily describes the stresses calculated using Eq. [2], leads to infer that consideration of M as 1.62 appears reasonable. However, the magnitude of Taylor's factor (M) as 1.62 is difficult to justify scientifically for BCC materials. It may be considered that the magnitude of Taylor's factor (usually 3.0) in Eqs. [2] and [6] could have a multiplier (~0.54), which makes the present estimate of M as 1.62; the physical meaning of the multiplier needs to be examined in a future investigation. Equation [6] predicts early saturation of the stresses as indicated in the Stage-IIIa for the SA600 specimen (Figure 15(b)). Thus, Eq. [6] involving dislocation–dislocation interaction does not satisfactorily describe Stage-III over the entire stress region. This might be due to the fact that the dependence of dislocation mean free path on dislocation density is not followed because of closely spaced second-phase α-particles. Estrin–Mecking[25] considered the mean free path as constant for particle-strengthened or fine-grained material; the mean free path for these microstructures is considered as the particle spacing or the fine grain size. In the present study, the dislocation mean free path can be described

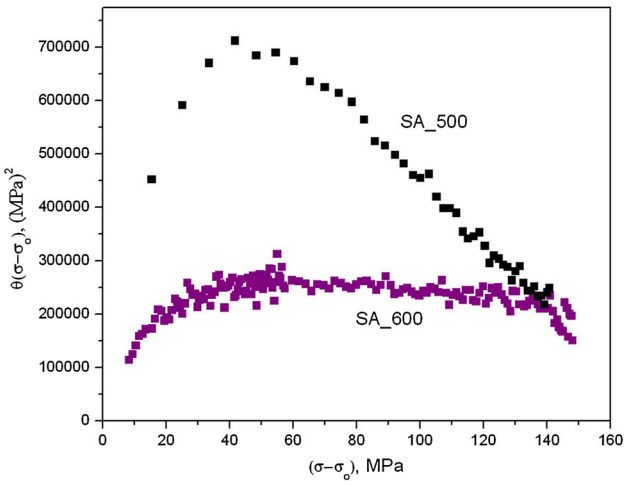

Fig. 16—Plots of $\theta(\sigma - \sigma_o)$ *vs* $(\sigma - \sigma_o)$ for SA500 and SA600 specimens.

by the inter-α-spacing and net evolution of dislocations can be expressed as

$$\frac{d\rho}{d\varepsilon_P} = M\left(\frac{1}{bL} - k_2\rho\right), \qquad [8]$$

where L is mean free path of a dislocation, which equates to the spacing (λ) between the α-phases.

The inter-α-spacing/cell size is either finer (in the SA500 specimen) or of the same order to that of dislocation mean free path for dislocation–dislocation interaction in the investigated aged conditions and hence Eq. [8] should be applicable for all these specimens.

One can note the major difference between K–M (in which the dislocation mean free path is inversely proportional to $\rho^{1/2}$) and E–M model (in which dislocation mean free path is constant) is related to the fact that the plot of $\theta(\sigma - \sigma_y)$ against $(\sigma - \sigma_y)$ passes through origin in the former, whereas it cuts the ordinate with some significant value for the latter. Figure 16 reveals that $\theta(\sigma - \sigma_y)$ *vs* $(\sigma - \sigma_y)$ plot for the SA500 sample (with smaller inter-α-spacing) yields considerable intercept, whereas the plot for the SA600 specimen (with relatively larger inter-α-spacing) shows a negligible intercept. These intercepts are inversely proportional to the particle spacing as proposed by the E–M model.[25]

Further, integration of the Estrin–Mecking expression [Eq. [8]) and subsequent substitution in Eq. [5] results in

$$(\sigma - \sigma_o) = kMGb\left[\frac{1}{bk_2L}\{1 - \exp(-k_2M\varepsilon)\} + \rho_o \exp(-k_2M\varepsilon)\right]^{1/2}, \quad [9]$$

where the parameters are similar to those stated earlier. The last term of Eq. [9], *i.e.,* $\rho_o \exp(-k_2M\varepsilon)$, can be neglected following the same reason given for ρ_o in Eq. [6]. The values of the k_2 for the aged conditions are determined from the slope of linear Stage-III regions as illustrated in Figure 16. Considering the values of L as inter-α-spacing (Table II), estimated values of $(\sigma - \sigma_o)/G$ from Eq. [9] are plotted in Figure 15(b) with the experimental results. The predicted values with $M = 1.62$ agree well with the experimental results for the alloy aged at both 773 K and 873 K (500 °C and 600 °C). This implies that for a finer microstructure in the presence of second-phase particles, the Estrin–Mecking model in Eq. [8] better describes the work hardening than the KM model in Eq. [3]. But, it should be kept in mind that the observed deformation of the α-phase in the latter stages of SA600 sample is not considered here for describing the E–M model for this aged condition.

V. CONCLUSIONS

1. Theoretical calculations of the volume fraction of α-phase in Ti-15-3 alloy using ThermoCalc software indicate a decrease in content with an increase in aging temperature from 773 K to 873 K (500 °C to 600 °C). Quantitative microscopy and XRD results support the above trend. The discrepancy in the estimated volume fraction of the α-phase determined by theoretical and experimental approaches is attributed to the consideration of equilibrium in theoretical calculation and its absence in the generated microstructure.
2. The strength and elastic modulus of the alloy deteriorated and the ductility improved at higher aging temperatures based on the size of the α and the extent of the α–β interface; at a higher aging temperature, the coarsening of α occurs with a concomitant decrease in the inter-α-spacing.
3. The yield strength of the aged alloys increases with a decrease in the inter-α-spacing. The dependency of yield strength on inter-α-spacing can be qualitatively described by the Meyer–Ashworth relationship.
4. The specimens aged at higher temperature reveal a change in the deformation behavior due to the deformation of α at higher plastic strains, but alloys aged at low temperatures do not indicate such deformation in the α-phase. It is considered that the deformation is governed significantly by the characteristics of inter-α-spacing.
5. Analyses of the work hardening behavior of the investigated alloy indicate that for a fine two-phase α–β structure the Estrin–Mecking model better describes the deformation behavior than that by the Kocks–Mecking model.

ACKNOWLEDGMENTS

The authors are thankful to DRDO for funding this research activity and also would like to thank the Director, DMRL, Hyderabad for his encouragement and permission to publish these results.

REFERENCES

1. R.R. Boyer: *Beta Titanium Alloys in the 1990's*, D. Eylon, R.R. Boyer, D.A. Koss, eds., TMS, Pennsylvania, 1993, p. 335.
2. P.J. Bania, G.A. Lenning, and J.A. Hall: *Beta Titanium Alloys in the 1980's*, R.R. Boyer, H.W. Rosenberg, eds., The Metallurgical Society of AIME, Pennsylvania, 1984, p. 209.
3. O.M. Ivasishin, P.E. Markovsky, Y.V. Matviychuk, S.L. Semiatin, C.H. Ward, and S. Fox: *J. Alloy. Compd.*, 2008, vol. 457, pp. 296–309.
4. N. Niwa, A. Aral, H. Takator, and K. Ito: *ISIJ Int.*, 1991, vol. 31, pp. 856–62.
5. T. Inaba, K. Ameyama, and M. Tokizane: *ISIJ Int.*, 1991, vol. 31, pp. 792–98.
6. T. Makino, R. Chikaizumi, T. Nagaoka, T. Furuhara, and T. Makino: *Mater. Sci. Eng. A*, 1996, vol. 213, pp. 51–60.
7. M. Okada: *ISIJ Int.*, 1991, vol. 31, pp. 834–39.
8. H. Fujii and H.G. Suzuki: *Beta Titanium Alloys in the 1990's*, D. Eylon, R.R. Boyer, D.A. Koss, eds., TMS, Pennsylvania, 1993, p. 249.
9. J. Ma and Q. Wang: *Mater. Sci. Eng. A*, 1998, vol. 243, pp. 150–54.
10. M. Okada, D. Banerjee, and J.C. Williams: *Titanium Science and Technology-Proceedings of the Fifth International Conference on Titanium Congress-Center*, G. Lutjering, U. Zwicker, and W. Bunk, eds., FRG, Munich, 1984, pp. 1835–42.
11. Y. Kawabe and S. Muneki: *ISIJ Int.*, 1991, vol. 31, pp. 785–91.
12. G. Qiang, W. Qing, S. Dong-Li, H. Xiu-Li, and W. Gao-Hui: *Mater. Sci. Eng. A*, 2010, vol. 527, pp. 4229–32.
13. G. Lutjering and J.C. Williams: *Titanium*, 2nd ed., Springer, Berlin, 2007, p. 16.
14. D.C. Ludwigson: *Metall. Trans.*, 1971, vol. 2, pp. 2825–28.
15. R.E. Reed-Hill, W.R. Cribb, and S.N. Monteiro: *Metall. Trans. A*, 1973, vol. 4, pp. 2665–67.
16. Y. Tomita and K. Okabayashi: *Metall. Trans. A*, 1985, vol. 16, pp. 865–72.
17. R. Sarkar, P. Ghosal, T.K. Nandy, and K.K. Ray: *Phil. Mag.*, 2013, vol. 93, pp. 1936–57.
18. M.A. Meyers and E. Ashworth: *Phil. Mag. A*, 1982, vol. 46, pp. 737–59.
19. J.G. Sevillano, P.V. Houtte, and E. Aernoudt: *Prog. Mater Sci.*, 1980, vol. 25, pp. 69–134.
20. U.F. Kocks and H. Mecking: *Prog. Mater Sci.*, 2003, vol. 48, pp. 171–273.
21. G.T. Terlinde, T.W. Duerig, and J.C. Williams: *Metall. Trans. A*, 1983, vol. 14, pp. 2101–15.
22. M.F. Ashby: *Strengthening Methods in Crystals*, A. Kelly and R.B. Nicholson, eds., Applied Science Publishers Ltd., London, 1971, p. 137.
23. I. Gutierrez and M.A. Altuna: *Acta Mater.*, 2008, vol. 56, pp. 4682–90.
24. C. Mondal, A.K. Singh, A.K. Mukhopadhyay, and K. Chattopadhyay: *Mater. Sci. Eng. A*, 2013, vol. 577, pp. 87–100.
25. Y. Estrin and H. Mecking: *Acta Metall.*, 1984, vol. 32, pp. 57–70.